# Aerosol-Assisted Production of Mesoporous Titania Microspheres with Enhanced Photocatalytic Activity: The Basis of an Improved Process

**Paula Z. Araujo,**[†] **Vittorio Luca,**[†,‡] **Patricia B. Bozzano,**[§] **Hugo L. Bianchi,**[†,||,⊥]
**Galo Juan de Ávila Arturo Soler-Illia,**[*,†,||,#] **and Miguel A. Blesa**[†,||,#]

Gerencia Química and Gerencia de Materiales, Comisión Nacional de Energía Atómica, Avenida Gral. Paz 1499, B1650KNA San Martín, Buenos Aires, Argentina, Institute of Materials Engineering, Australian Nuclear Science and Technology Organisation, New Illawarra Road, Lucas Heights NSW 2234, Australia, Consejo Nacional de Investigaciones Científicas y Tecnológicas, CONICET, Buenos Aires, Argentina, and Escuela de Ciencia y Tecnología and Instituto de Investigación e Ingeniería Ambiental (3IA), Universidad Nacional de San Martín, San Martín, Buenos Aires, Argentina

**ABSTRACT** An aerosol-based process was used to prepare mesoporous $TiO_2$ microspheres (MTM) with an average diameter in the range of 0.5−1 $\mu$m. The structural characteristics and photocatalytic properties of the synthesized materials were determined. As-prepared MTM materials and those heated in air from 400 to 600 °C exhibited mesoporous texture with a narrow size distribution and an inorganic framework that consisted of 4−13 nm anatase crystallites. Pore volumes for the MTM materials were in the range of 0.17−0.34 $cm^3\ g^{-1}$. Microspheres heated to 400 °C presented a locally ordered mesopore structure and possessed X-ray diffraction *d* spacings between 9.8 and 17.3 nm. Heating above 400 °C resulted in a loss of the mesoscopic order, a decrease of the surface area, retention of the porosity, and an increase of the anatase nanoparticle size to 13 nm. The accessibility of the pore volume was measured by monitoring the uptake of gallic acid (GA) using Fourier transform IR. The MTM materials made excellent catalysts for the photodegradation of GA, with the performance being higher than that of an equivalent sample of Degussa P25. The present MTM materials are advantageous in terms of their ease of separation from the aqueous phase, and hence a novel photocatalytic process is proposed based on separate adsorption and photocatalytic decomposition steps with an improved and more rational use of both catalyst and sunlight.

**KEYWORDS:** mesoporous • photocatalysis • photodegradation • microspheres • titania • aerosol

## INTRODUCTION

In 1972, Fujishima and Honda demonstrated the photoelectrolysis of water using $TiO_2$ semiconductor anodes to produce hydrogen and oxygen (1). The potential demonstrated by this initial result spawned intense investigation devoted to the development of $TiO_2$-based water photoelectrocatalysis and heterogeneous photocatalysis (HP) for the destruction of organic pollutants in air and water (2−6). The efficiency of HP in water is lower than that in the gas phase (7, 8). This low efficiency represents a significant limitation in the development of commercial-scale technologies.

Much effort has also been expended in the use of direct solar illumination to decontaminate and disinfect water (9−11). Solar HP (SHP) holds promise as a practical technology that can be demonstrated at the commercial scale (12, 13). However, this promise has not yet been fully realized because of the weak overlap of the $TiO_2$ fundamental absorption edge with the solar spectrum, suggesting that even at 100% quantum efficiency less than 5% of the incident light energy can be utilized (14). In other words, only the UV-A fraction of the solar spectrum can be utilized by $TiO_2$ photocatalysts. Of course, the quantum efficiency is actually much less than 100% because of the short lifetime of the charge carriers; therefore, the effectiveness of $TiO_2$-based photocatalysts is rather limited. A much investigated strategy for improving the performance of $TiO_2$ photocatalysts has been to extend the band-gap absorption into the visible region by cation (15, 16) and, more recently, anion doping of the semiconductor (17, 18). However, such approaches have generally met with limited success possibly because carrier life times may be decreased by the pollutants to be destroyed (19). Therefore, close contact between the semiconductor and pollutant is required if charge separation is to compete favorably with charge recombination. This

---

[*] To whom correspondence should be addressed. E-mail: gsoler@cnea.gov.ar.

Received for review March 5, 2010 and accepted May 21, 2010

[†] Gerencia Química, Comisión Nacional de Energía Atómica.

[‡] Australian Nuclear Science and Technology Organisation.

[§] Gerencia de Materiales, Comisión Nacional de Energía Atómica.

[||] CONICET.

[⊥] Escuela de Ciencia y Tecnología, Universidad Nacional de San Martín.

[#] Instituto de Investigación e Ingeniería Ambiental, Universidad Nacional de San Martín.

DOI: 10.1021/am100188q

requirement sets stringent limitations on the design of solar photocatalytic reactors (20). The natural fluctuations in available solar radiation on the surface of the earth impose still further limitations on the efficiency of the photodegradation process (21). In addition, two further shortcomings arise regarding the use of commercial nanoparticle dispersions such as P25 including (a) a reduced effective active surface due to aggregation and (b) a difficulty in separating the catalyst from the liquid media to be treated.

A possible means to overcome these shortcomings involves the separation of the heterogeneous photocatalytic process into two steps. The first step would involve removal of the pollutant species from the aqueous phase by an adsorption process in the absence of light, and the second step would be the HP destruction. For this purpose, the ideal photocatalyst should have accessible pore surfaces and high adsorption capacity and be easily separated from solution. This process is not more complex than the traditional direct irradiation of slurries that ultimately requires a subsequent separation. Procedures using supported catalysts have, on the other hand, met with some success, although they suffer from the very limited surface area of the semiconductor and sluggish mass-transport kinetics (22).

Mesoporous titania with a stable high surface area, controlled mesoporosity, and a nanocrystalline framework offers tremendous potential in this field, and improved photocatalytic properties are expected for systems that allow an efficient electron transfer and a high pollutant adsorption at the same time. Essentially two routes toward this target have been reported in which the mesoporosity is due to either textural effects or the use of template molecules. In the first case, the pores originate from the voids after nanoparticle packing. In the second case, mesopores stem from the elimination of the template. Indeed, photocatalysis has helped to spur research in what has become the very active field of non-silica mesoporous materials. Several methods have been presented that led to highly active mesoporous titania on the laboratory scale (23−26). In the case of templated titania, the evaporation-induced self-assembly (EISA) route (27) is more reliable and reproducible than that based on precipitation (28−30). In particular, aerosol-based methods have proven to be suitable for obtaining a great variety of highly controlled mesoporous materials. In addition, aerosol synthesis can be easily adapted to EISA and scalable, opening the possibility of obtaining large quantities of powder with high purity and uniform pore structure for practical applications, affording a reduction in the number of operations (31). Although aerosol methods have been mostly applied to silica systems, the inclusion of titania nanoparticles has been achieved (32, 33), resulting in photocatalytically active composites (34). However, the agglomeration of the titania nanoparticles can limit the photocatalytic performance of the ensemble, making the production of pure mesoporous titania desirable (35, 36).

The present contribution describes the synthesis and characterization at the laboratory scale (in a grams per day yield) of micrometer-sized mesoporous $TiO_2$ spheres with high surface areas, highly controlled mesopore sizes, and interconnectivity and an anatase framework with a controllable crystallite size. The adsorptive and photocatalytic properties of these materials were explored using gallic acid (3,4,5-trihydroxybenzoic acid, GA) as a model pollutant (37−42).

The aim of this work is to characterize the structure and photocatalytic activity of crystalline mesoporous titania microspheres and to determine if a viable alternative process can be contemplated for effecting the photocatalytic decomposition of model pollutants. A correlation is observed between the photocatalytic properties and the nanometric size of pores and interpore necks and the anatase crystallite size; the optimized performance is a consequence of tuning the thermal treatment. As-prepared materials present high surface areas and mesopores and inorganic walls formed by a small-size anatase, with a low photocatalytic effect. A postprocessing thermal treatment step at $T > 400$ °C leads to lower surface area, a mesopore size increase, and higher crystallinity, leading to equivalent to superior photocatalytic activity when compared to the P25 powder.

## EXPERIMENTAL SECTION

**Synthesis of Mesoporous Titania Microspheres (MTMs).** MTMs were prepared using an aerosol method, conceptually similar to that previously described (31, 32, 35). The microspheres were obtained through the controlled evaporation (EISA) of nebulized droplets from an initial sol in a tubular furnace (see below). Aerosols were generated by a piezoelectric device (see below). Initial sols were made from an alcohol−water solution containing inorganic precursors and polymeric templates. The inorganic precursor was prepared by hydrolysis and condensation of $TiCl_4$ in the presence of controlled water quantities.

Initial sols were prepared at room temperature by adding $TiCl_4$ (Merck) to ethanol under vigorous stirring; this step should be undertaken carefully on an ice bath because of the exothermic alcoholysis of the chloride that releases HCl vapors. This first $TiCl_4$−EtOH solution was then added slowly under continuous stirring to an alcoholic solution that contained a structure agent and deionized water. The nonionic triblock copolymer Pluronics F127 ($EO_{106}PO_{70}EO_{106}$, Sigma) was used as the structure-directing agent. The starting solution composition was chosen to permit nebulization; several experiments were carried out in order to determine the best conditions, which turned out to be similar to those used in the preparation of films (43). The optimum final molar ratio ($TiCl_4$−$H_2O$−$CH_3CH_2OH$−F127) was found to be 1:26:187:0.005.

The reactor construction used for microsphere production was inspired by a design presented by Baccile et al. (32). Similar reactors have also been reported by other authors (31, 44, 45). Iskandar et al. (46) demonstrated that the droplet size could be controlled by setting the frequency of the ultrasound generator of the nebulizer (46). In our case, a commercial 1.7 MHz piezoelectric crystal was used, and this was located in the bottom of a 10 mL chamber contain-

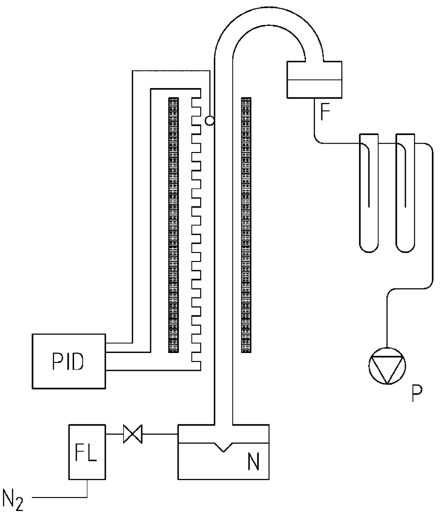

**FIGURE 1. Apparatus sketch: N, nebulizer; PID, temperature controller; P, gas pump; F, filter (set at 85 °C); FL, nitrogen flow control.**

ing the precursor solution. MTMs were generated under homogeneous and constant laminar nitrogen flow (INDURA, 99.999%; 0.5 $dm^3\ min^{-1}$) to avoid alcohol combustion (42). The spherical drops generated by the ultrasonic nebulization procedure enter an externally heated quartz columnar reactor with an internal diameter of 20 mm and a length of 80 cm and set at 350 °C. The residence time of the aerosol in the reactor was estimated at 30 ± 1 s by measuring visually the time in which a recently generated aerosol cloud passed through the column. This is in good agreement with the nominal nitrogen flux. The aerosol is thus exposed to a steep temperature gradient (25−350 °C) in 30 s. An inline filter was used to collect the MTM powder after the reactor (F in Figure 1). This filter is maintained at 85 °C in order to eliminate the presence of chloride in the final material. Two successive traps, one with NaOH and the other one an empty trap, in thermal contact with liquid nitrogen, were used to eliminate HCl and remnant alcohol. A vacuum pump provided a constant flow regime (see Figure 1). The as-synthesized MTM samples were directly obtained from this setup, with a yield of ca. 100 mg $h^{-1}$ of mesoporous material (see below). This implies that less than 90 mg of the aerosol are present within the active volume of the reactor during the fixed residence period. Thermal treatment of the as-prepared MTM sample was performed by heating the powder with a ramp of 1 °C $min^{-1}$ up to 400, 500, or 600 °C. Once the target temperature was attained, it was maintained for 2 h. A residual organic template was also removed during this dwell stage. The thermally treated $TiO_2$ microsphere samples will be designated as MTM-*x*, where *x* represents the calcination temperature in degrees Celsius.

Commercial titanium dioxide (Degussa P25) without further purification was used as a benchmark for the photocatalytic activity. P25 is composed mainly of anatase (ca. 75%) and rutile (ca. 25%). The modal particle size is ca. 25 nm, and its Brunauer−Emmett−Teller (BET) specific area is 51.4 $m^2\ g^{-1}$. All other reagents were analytical grade and were used as received. All solutions were prepared with deionized water from an E-pure equipment.

**Characterization.** Scanning electronic microscopy (SEM) images were obtained using a Philips 515 instrument. Particle size distributions were determined from the micrographs using *Image J* software.

Template elimination was checked by Fourier transfer infrared (FTIR) spectroscopy. FTIR spectra were recorded on a Nicolet MAGNA 560 instrument equipped with a liquid-nitrogen-cooled MCT-A detector. This equipment was used in all FTIR measurements.

X-ray diffraction (XRD) patterns were acquired on a Scintag X1 instrument using Cu K$\alpha$ radiation and $\theta-\theta$ geometry. This instrument was operated with a 270 mm goniometer radius and was fitted with a Peltier-cooled detector (47). The crystal size was estimated by applying the Scherrer equation. Potassium chloride was used as a standard for determination of the instrumental line broadening.

Nitrogen adsorption−desorption isotherms were recorded at 77 K using a Micromeritics ASAP 2010 instrument. The specific surface area and porosity evaluation were calculated using BET and Barrett−Joyner−Halenda (BJH) models, respectively. All samples were degassed between 100 and 150 °C prior to measurement.

Transmission electron microscopy (TEM) images were recorded using a Philips CM200 Super Twin instrument operated at 200 kV. Powder or microtomed particles, fixed using an Epoxy Embedding medium kit (Fluka), were deposited on FORMVAR-coated copper or gold grids. Dark-field mode was used to characterize the crystalline domains, and small-angle XRD was used to probe the ordering of the pore network.

**Accessibility of the Pore System.** Dihexadecylphosphate (DHDP), with long aliphatic chain molecules, was used to evaluate the accessibility of the pore system, as reported in ref 43. The mesoporous titania powders were suspended in a 0.01 mol $dm^{-3}$ DHDP solution in tetrahydrofuran (THF; 0.6 g $dm^{-3}$ $TiO_2$) and stirred for specified times. The suspensions were centrifuged (3500 rpm and 4 min), the supernatant was removed, fresh THF was added, and the procedure was repeated twice. FTIR spectra of the solid in KBr pellets were recorded with 200 scans and 4 $cm^{-1}$ resolution.

**Model Pollutant Adsorption and Photocatalytic Degradation.** The adsorption capacity for GA was measured as described (42). Thin colloidal films were deposited on an attenuated total reflectance (ATR) crystal surface by placement of 0.150 $cm^3$ of the MTM-*x* or P25 suspensions (20 g $dm^{-3}$) and by careful evaporation to dryness inside a desiccator at room temperature. The $TiO_2$ films thus formed were then rinsed with water to eliminate loosely deposited particles, and a freshly prepared solution of $1 \times 10^{-4}$ mol $dm^{-3}$ GA in $1 \times 10^{-2}$ mol $dm^{-3}$ KCl (1.8 mL) was applied to the $TiO_2$ film supported on the ATR crystal (ZnSe substrate). In order to follow GA adsorption, ATR-FTIR spectra were recorded as a function of time at room temperature until no further changes were detected. This indicated that the surface film had been saturated with the adsorbent. Typically, equilibration times were on the order of 60 min. The incidence angle of the Spectra Tech horizontal ZnSe−ATR unit (area = 10 × 72 mm$^2$) was 45°, and the total number of reflections was 11. Spectra were taken with 200 scans and 4 cm$^{-1}$ resolution, the background was subtracted, and a baseline correction was made for instrumental instabilities. At the end of each experiment, the UV−vis spectrum of the remnant solution was recorded in a diode-array Hewlett-Packard 8453 apparatus.

In situ determination of the reactants and products during photocatalysis experiments was performed on the GA-containing titania films previously deposited on the ATR crystal. Each isolated film was exposed to a 15 W, 365 nm UV lamp (F15T8BLB Black Light Blue Fluorescent, Eiko), and sequential ATR-IR spectra were taken at defined intervals. As shown below (Figure 9), the action spectrum of the lamp is a band centered at 350 nm, with a half-height width of 50 nm. The total radiation incident on the film, measured by chemical actinometry (48) with potassium ferrioxalate, was 5.46 × 10$^{16}$ photons s$^{-1}$. The band area between 1419 and 1272 cm$^{-1}$, assigned to $\nu_s(CO_2^-)$ and $\nu$(Ph−O), (49) was chosen in order to follow the changes in the GA surface excess.

## RESULTS AND DISCUSSION

### Characterization of MTMs.

All particles obtained by the aerosol method were spherical, with diameters typically in the range of 0.05−5 $\mu$m. Despite the low residence time in the reactor (around 30 s), the as-synthesized materials, MTM-25, were found to be template-free by FTIR (see Figure S1 in the Supporting Information). This fact might seem surprising at first sight. However, as stated above, in the flow and aerosol dispersion conditions presented here, ca. 10 g of a dilute solution is processed every 1 h. This means that less than 90 mg of the precursor solution is continuously present in the reactor chamber, which is kept at 350 °C. The energy needed to heat and evaporate the solvent and heat the material thus formed to its final temperature can be roughly estimated to be less than 200 J, implying the use of less than 10 W of power. Therefore, it can be safely stated that the samples reach a temperature where the template can be decomposed within the residence time.

Further thermal treatment did not affect appreciably the morphology. Shown in Figure 2 are the SEM and TEM images of the microspheres after heating at 400 (Figure 2a,b) and 600 °C (Figure 2c,d). The SEM images of both samples clearly reveal spherical particles with a large degree of polydispersity, as exemplified in the histogram obtained from analysis of the SEM images of an MTM powder heated at 500 °C (Figure 2e). It is also apparent that the particle shape remains invariant regardless of the temperature. A comparison of the particle size histograms obtained from analysis of the SEM micrographs does not lead to significant differences in the average distributions, although samples treated at higher temperatures seem to be slightly smaller, possibly because of contraction upon heating, as a consequence of densification. TEM examination of the MTM-400 sample shows that all of the spheres display an array of regular mesopores, locally ordered along the particle radius. Electron diffraction of zones of the sample confirmed the presence of nanocrystallinity (see below) in the as-synthesized materials. For the sample heated at 600 °C, denser inorganic walls are evident, and mesopores are still observed, somehow less ordered and more polydisperse compared to the lower temperature samples. Each microsphere batch treated at higher temperatures is, in fact, composed of partially sintered nanoparticles or nanocrystallites, and the pore voids between them reflect the combined effect of the supramolecular templating and the process of crystallite growth and reorganization that take place upon heating.

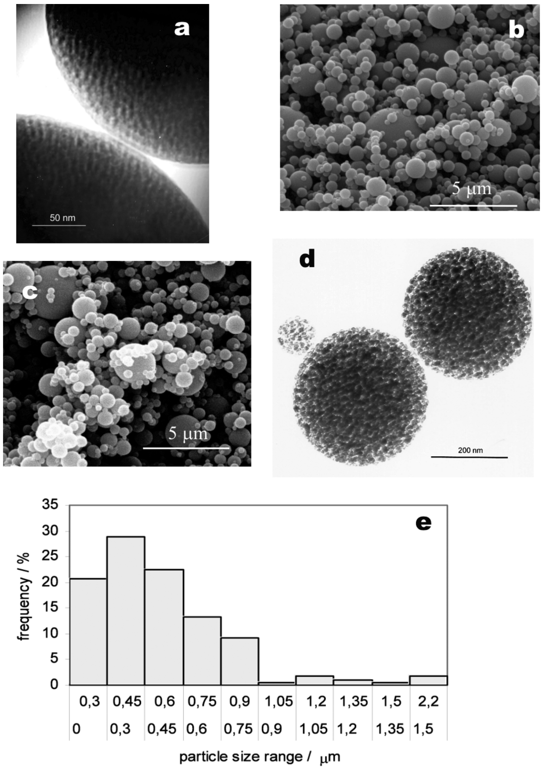

**FIGURE 2. TEM and SEM images of the aerosol-generated MTM-400 (a and b) and MTM-600 (c and d). Particle size distribution histograms for the MTM-500 sample (e).**

Low-angle diffraction patterns of the series of samples are shown in Figure 3A; MTM-25 and MTM-400 display low-angle reflections with *d* spacings of about 17.3 and 9.8 nm, respectively. The low-angle diffraction signals are typical of templated mesopore systems, in which at least a local pore correlation is present. It has also to be acknowledged that a loose packing of relatively monodispersed nanoparticles can lead to the observation of low-angle reflections corresponding to texture (50). However, in this case the nanoparticle sizes do not correlate with the observed distances (see below), reinforcing the hypothesis of a templating effect due to the F127 polymer. The low-angle reflections due to mesopore order were no longer evident in samples calcined at 500 and 600 °C. The disappearance of low-angle reflections with increasing temperature is in agreement with TEM observations that suggested a loss of pore and/or nanoparticle correlation accompanied by anatase nanoparticle growth (51−53).

The structural evidence presented so far indicates that porous templated titania microspheres are obtained through

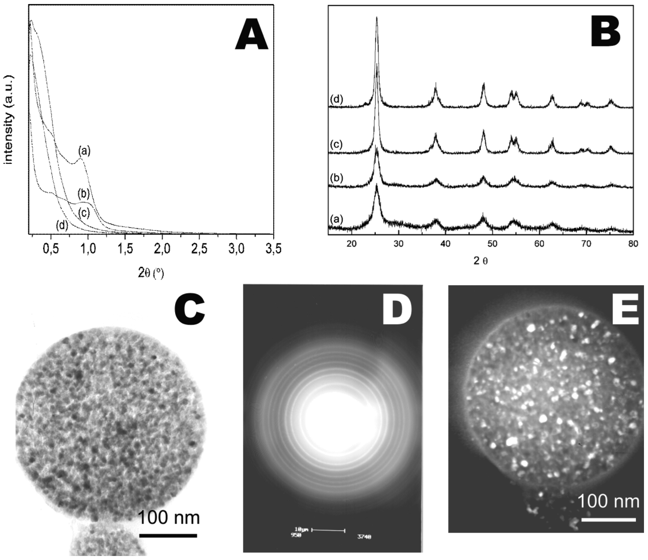

**FIGURE 3. Low- (A) and wide-angle (B) XRD patterns of (a) MTM-25, (b) MTM-400, (c) MTM-500, and (d) MTM-600. TEM micrographs of an MTM-500 sample: bright-field image (C), SAED pattern (D), and dark-field image (E).**

an EISA-like process. The features observed in the MTM-25 sample (locally ordered mesopores and removal of a large fraction of the template) can be attributed to rapid energy transfer to the particles, due to the reactor temperature and the small quantities of sample involved. These conditions lead to the fast evaporation of solvent (ethanol−water) from the initially formed droplets; this drying event triggers ordering (29b). According to previous work, the solvent evaporation process can take a few seconds (54). Optimization of the EISA conditions implies the careful balance of the rates of solvent volatilization and inorganic condensation, which also increases with the temperature. Volatilization of the condensation inhibiter (HCl), which is likely to occur at a slower rate than that of the solvent (29b), is also likely to have an impact on the self-assembly process. These factors are critical in attaining ordered or monodisperse templated mesopores (27, 29, 55−58). Indeed, recent in situ experiments on mesoporous aerosols have shown that the formation of an ordered mesostructure can be attained within residence times and temperatures comparable to those presented here (59). In the conditions reported in our work, both rates are well balanced: even if the high temperature gradient imposes a large driving force for drying, the presence of large quantities of HCl in the initial sols (from $TiCl_4$ hydrolysis) hinders the extended condensation process of Ti−O moieties. This synthetic tailoring assists the correct coassembly of the F127 template and the inorganic components and the formation of mesopores even in the apparently short residence times. In addition, the temperature reached at the end of the reactor is in our case high enough to decompose the template at least to some extent, as proven by FTIR. In previous works, it has been observed that shorter residence times or lower oven temperatures lead to template-containing mesostructured materials (32). Thus, the preparation conditions of MTM-25 have made it possible to obtain a virtually template-free mesoporous material through a simple and continuous process.

**Table 1. Porosity and Structure Characteristics of MTM-*x* Samples**

| heat treatment temperature [°C] | surface area [m$^2$ g$^{-1}$][a] | average pore size[b] [nm] | average neck size[c] [nm] | pore volume[a] [cm$^3$ g$^{-1}$] | CSD [nm] |
|---|---|---|---|---|---|
| P25 | 50 | | | | 25 (R),<br>80 (A) |
| as-prepared | 294.1 | 4.9 | 3.9 | 0.38 | 4.8 |
| 400 | 207.8 | 4.2 | 3.5 | 0.23 | 6.74 |
| 500 | 73.1 | 7.8 | 7.0 | 0.17 | 11.7 |
| 600 | 69.8 | 8.0 | 7.1 | 0.17 | 11.5 |

[a] BET. [b] From the BJH adsorption branch. [c] From the BJH desorption branch.

The wide-angle diffraction patterns of the series of samples (Figure 3B) correspond to nanocrystalline anatase and confirm that this phase is obtained at all temperatures, even for the as-prepared sample. The average crystallite sizes were calculated from the anatase (101) XRD peak full width at half-height using the Scherrer equation; detailed results are reported in Table 1. The as-synthesized materials (MTM-25) comprise anatase nanocrystalline walls with an average crystallite diameter of 4.8 nm. Upon calcination at 400 °C, these anatase crystallites grew, eventually reaching a final size in the range of 11−12 nm for both MTM-500 and MTM-600. This is in very good agreement with the TEM information in that selected area electron diffraction (SAED) showed anatase diffraction patterns in all cases (Figure 3C). In addition, dark-field TEM images showed the presence of nanocrystallites throughout the samples (Figure 3D). In conclusion, the microsphere walls that are generated consist of nanometric anatase domains of variable size, with larger nanocrystallites being formed at higher temperatures. Crystallite sizes estimated from TEM images were in good agreement with those obtained from Scherrer analysis of the XRD patterns and showed well-defined nanocrystallites with angular faceting (ca. 11 × 11 nm square section for the 600 °C sample). It can also be seen that the pore network interconnection was improved in the thermally treated materials; i.e., interpore necks were observed.

The preceding structural data are consistent with the porosity results shown in Figure 4, where features typical of mesoporous materials are observed for all samples. This was deemed to be a consequence of supramolecular pore templating. All MTM-*x* materials presented type IV nitrogen adsorption−desorption isotherms with inflections due to capillary condensation at $P/P_0$ between about 0.4 and 0.8 (Figure 4a). All of the adsorption−desorption isotherms and their associated type H2 hysteresis loops were very similar to those observed in the case of nanocrystalline anatase powders (50). As the temperature at which the MTM materials were calcined was increased, three main features were observed: (a) the overall surface area decreased, (b) gas adsorption at low pressures diminished, reflecting a loss of microporosity, and (c) the inflection moved to higher $P/P_0$ values, indicating an increase in the mesopore dimension, while the hysteresis loop remained unchanged. It is clear that

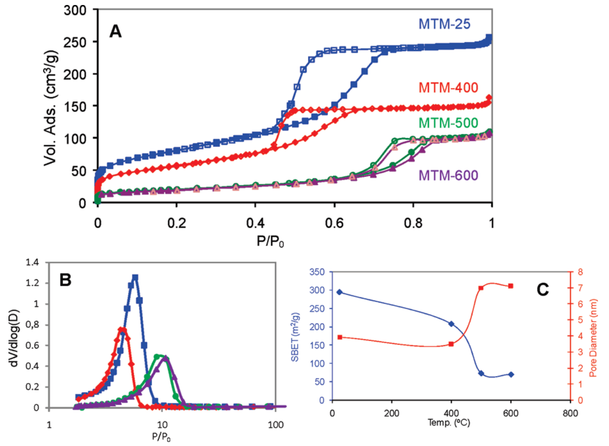

**FIGURE 4. Nitrogen adsorption−desorption isotherms (A) and pore size distributions obtained from the adsorption branch by the BJH method (B) for MTM samples treated at different temperatures. (C) Evolution of the surface area and mesopore size for the MTM-*x* samples.**

as the samples were heated the specific surface area and microporosity were modified significantly, while only relatively minor modifications were observed in the mesopore texture. Table 1 summarizes the structural and textural results obtained. The BET surface areas of MTM-25 and MTM-400 were of the same order of magnitude as those previously reported for organized mesoporous titania (29); treatment at higher temperature resulted in surface areas comparable to those of conventional titania nanocolloids and on the order of 50−70 m$^2$ g$^{-1}$. The low-temperature samples also showed considerable microporosity, the origin of which is the likely result of the interpenetration of the F127 and Ti−O building blocks at the template−inorganic interface, as is well-known in block-copolymer-templated oxides (55, 60). In this particular case, the strong F127−titania interactions and the fast evaporation rate during the residence time in the aerosol reactor can favor the development of a less dense titania framework. This microporosity largely disappeared at higher temperatures because of the extensive evolution of the inorganic walls (61). The adsorption isotherm shapes at all temperatures indicate the presence of mesopores characterized by a narrow size distribution; the modal sizes are shown in Table 1. Pore size distributions were calculated from the adsorption branch by the BJH method. A progressive pore size increase was observed as a function of the temperature with a significant step after treatment at 500 °C (Figure 4B). Commensurately, all of the desorption curves showed a sharp drop corresponding to the capillary evaporation interval. This behavior has been observed in ink-bottle mesopore systems above certain critical pressure and temperature values of the adsorbate. Current models consider that this lower pressure limit can be associated with the size of the smallest mesopores that still exhibit adsorption−desorption hysteresis. In the case of cagelike pores, this size correlates well with the mesopore entrances or "interpore necks" (62−64). Table 1 also shows this "interpore neck" diameter calculated by the BJH method from the desorption step of each sample. The observed trend is in line with the pore size, indicating that the pore entrances become progressively larger upon thermal treatment.

Evolution of the textural properties with thermal treatment (decrease in the surface area, pore and interpore neck size increases, and decrease of the microporosity) is shown in Figure 4C. It can be observed that, between the as-synthesized MTM-25 material and MTM-400, the surface area, pore volume, and mesopore size decrease, while anatase crystallites grew. Dramatic textural changes associated with the further growth of anatase crystallites take place between 400 and 500 °C, in agreement with the TEM and XRD observations. In this temperature interval, the extended anatase growth process leads to a marked pore coarsening: micropores are lost, the total pore volume decreases, and an increase in the mesopore and interpore sizes is observed. Between 500 and 600 °C, the pore volume and crystallite size remained practically constant, although some minor increase in the pore and interpore neck sizes proves that the inorganic skeleton is still dynamic and undergoes changes in order to optimize the energy balance of the high surface area versus the crystalline character of the framework.

It can be concluded that as-prepared MTM samples exhibit micro- and mesoporosity because of elimination of the surfactant within the reactor. Upon thermal treatment, gradual changes occur because of anatase crystallization and nanoparticle sintering in the mesoporous system below 400 °C. This leads to a more compact mesoporous framework that gradually loses microporosity. For higher temperatures, extended crystallization of anatase within the inorganic walls takes place and the mesoscopic texture evolves as the samples are increasingly heated. This crystal growth seems to occur while retaining the overall mesoporosity. The final mesoporous texture is derived from the templated pores created upon the EISA process and may be due to a restricted crystallization phenomenon taking place in the confined environments of the mesopore walls. This effect has been observed in anatase growth in mesoporous thin films where it has been advanced that the mesopore system geometry determines the final shape and size of the anatase nanocrystals. This is likely to be attributable to the rapid anatase nucleation followed by confined growth, the limits to which are set by the pore interfaces (65). Oriented growth and rearrangement occur because of these limitations, and the final pore and crystallite structures are intimately related to the low-temperature structures (66). In the present case, as a consequence of the thermal treatment, the surface area decreases as the pore and neck sizes increase (coarsening), resulting in a mesoporous, nanocrystalline, robust, and highly accessible titania framework. Importantly, anatase growth and eventual sintering seem to occur preferentially within the microparticles, leading to a stable nanocrystalline material that keeps the structure and topology of the original mesoporous system. In addition, wide interpore necks are produced as a consequence of this evolution toward minimal surface area at high temperatures. This feature imparts a high accessibility to the mesopore system, a clear advantage for catalytic purposes. Accessibility and extended pore in-

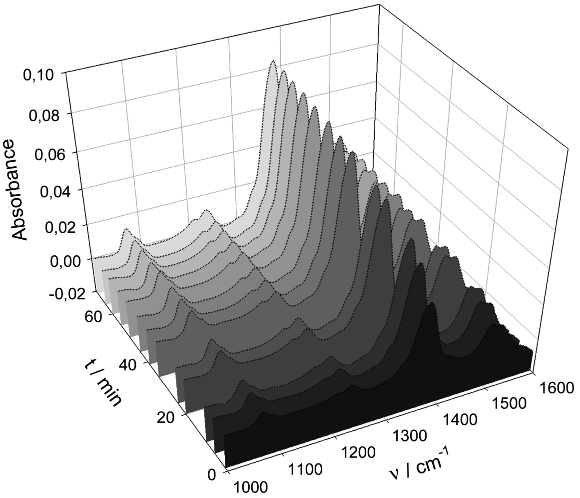

FIGURE 5. Series of ATR-FTIR spectra of GA adsorbed onto MTM-600 in the dark at pH 6.15 along the contact time, in the 1000−1600 cm$^{-1}$ region. Absorption bands of the adsorbate, $\nu_s$ (1380 cm$^{-1}$) and $\nu_a$ (1530 cm$^{-1}$), were attributed to ref 39.

terconnectivity were corroborated by measuring the incorporation of a bulky organic molecule, DHDP (67). FTIR spectra of MTM-400 exposed to a 0.01 mol dm$^{-3}$ DHDP solution in THF (see the Supporting Information) showed typical bands belonging to this molecule bound to the titania surface ($\nu_{C-H}$ in the 2900−3000 cm$^{-1}$ region, $\nu_{P=O}$ between 1100 and 1300 cm$^{-1}$, and $\nu_{P-O-C}$ in the 1000−1100 cm$^{-1}$ region) after contact times as short as 15 min.

**Model Pollutant Adsorption and Photocatalytic Degradation.** Adsorption onto a MTM-600 microsphere film from a solution containing [GA] = 1 × 10$^{-4}$ mol dm$^{-3}$ at pH 6.15 and $I$ = 1 × 10$^{-2}$ mol dm$^{-3}$ [KCl] is complete in about 1 h. The surface coverage (in mol g$^{-1}$) reached is similar to that reported for the standard reference material, Degussa P25 (42), indicating that not all sites in MTM-600 are available for GA adsorption because of either partial pore occlusion or the development of necks within certain regions of the pore system. These limitations have been previously observed in the diffusion of large molecules in titania xerogels (43).

The time span required to saturate the surface is typical of adsorption onto $TiO_2$ films and describes one of the important limitations of supported film-based photocatalytic reactors. In flow reactors, such as the SOLWATER reactor (9), the residence time of the solution in the illuminated tubes is much shorter (ca. 2 min for SOLWATER) than the time required to reach adsorption equilibrium. Figure 5 shows the time evolution of the FTIR spectrum of GA adsorbed onto an MTM-600 microsphere film in the conditions described above. FTIR peak assignments were taken from previous work (42). In the region around 1380 cm$^{-1}$, $\nu_s$ is seen at pH 6.15; overlapping the strong OH deformation vibration, $\nu_a$ is also seen at pH 6.15 as a shoulder at 1530 cm$^{-1}$.

Figure 6 shows the time evolution of the 1419−1272 cm$^{-1}$ band area, for comparable masses of MTM-600 and Degussa P25 (upper solid curve). The plot describes the time evolution of the degree of surface coverage, $\theta$ (measured as

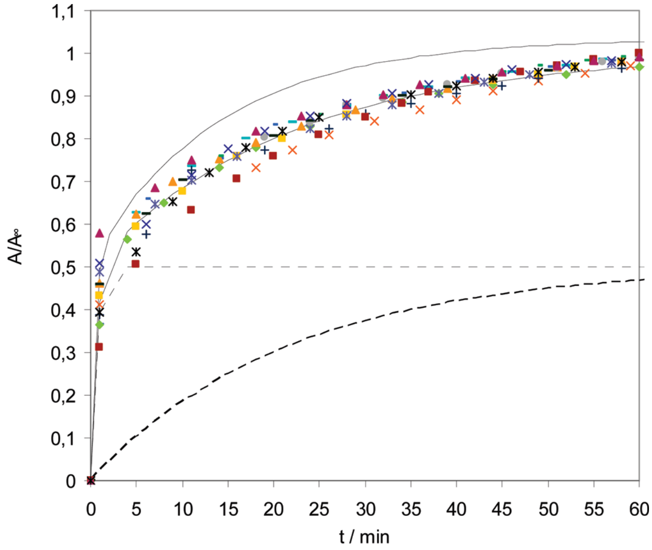

FIGURE 6. Time evolution of the integrated 1419−1272 cm$^{-1}$ area ($A/A_\infty$) for films in contact with an initial solution of 1 × 10$^{-4}$ mol dm$^{-3}$ GA at pH 6.15. Contributions Langmuir−Hinshelwood (− · · − and · · ·). Full lines represent the sum of all experimental points for P25 (upper solid line) and MTM-600 (lower solid line). Symbols of the same color represent a given adsorption curve on an independent sample.

the absorbance ratio $A/A_\infty$). The time evolution of $\theta$ was found to be very reproducible, although the adsorption capacity showed rather large variations in the individual experiments. This latter feature has been attributed to random changes in the fraction of the film that is really available for adsorption.

The kinetic profile in Figure 6 cannot be fitted with eq 1, corresponding to a simple Langmuir scheme, eqs 2 and 3:

$$d\{\equiv Ti-L\}/dt = k_1 N_s[HL] - (k_1[HL] + k_{-1})\{\equiv Ti-L\} \tag{1}$$

$$\equiv Ti-OH + HL \rightarrow \equiv Ti-L + H_2O; \quad k_d \tag{2}$$

$$\equiv Ti-L + H_2O \rightarrow \equiv Ti-OH + HL; \quad k_{-1} \tag{3}$$

Because the purpose of the present study was to compare the adsorption behavior of mesoporous titania and Degussa P25, we believe that it is not necessary to consider any more sophisticated and possibly more realistic descriptions of adsorption kinetics that include, for instance, (a) the possibility of both bulk (solution) and surface diffusion in pores (68), (b) concentration-dependent effective diffusion constants (69), (c) interplay between the empirical kinetic equation and diffusion or surface control (70a) or the two-resistance model for adsorption in porous particles (70b).

Instead, assuming two parallel Langmuir−Hinshelwood processes, the data can be adequately fitted; the integrated kinetic equation is eq 4.

$$\theta = \left(\frac{k_1(1)[\mathrm{HL}]}{k_1(1)[\mathrm{HL}] + k_{-1}(1)}\right)\{1 - \exp[-[k_1(1)[\mathrm{HL}] + k_{-1}(1)]]t\} + \left(\frac{k_1(2)[\mathrm{HL}]}{k_1(2)[\mathrm{HL}] + k_{-1}(2)}\right) \times \{1 - \exp[-[k_1(2)[\mathrm{HL}] + k_{-1}(2)]]t\} \quad (4)$$

Earlier work (42) had already shown that two Langmuir processes were required to describe adsorption of GA onto Degussa P25; interestingly, one Langmuir constant sufficed to describe the adsorption of GA onto Degussa P25 ($K_L = 5.04 \times 10^4$ dm$^3$ mol$^{-1}$ at pH 6.2). The data in Figure 6 can also be fitted using only one $K_L$ value and, assuming that the value derived for Degussa P25 also applies to MTM-600, is the same for both parallel pathways. A very good fit is obtained with $k_1(1) = 1.8 \times 10^4$ dm$^3$ mol$^{-1}$ s$^{-1}$, $k_{-1}(1) = 3.7 \times 10^{-1}$ s$^{-1}$, $k_1(2) = 5.2 \times 10^2$ dm$^3$ mol$^{-1}$ s$^{-1}$, and $k_{-1}(2) = 1 \times 10^{-2}$ s$^{-1}$. These values are, however, only indicative because the fitting procedure is not sensitive enough to observe changes in $K_L$, and the value for MTM-600 may differ from the value measured for P25. The conclusion remains, however, that two rate processes take place with very different characteristic times. These two processes have been assigned to adsorption onto readily available and less accessible film sites. Table 2 compares the kinetics of adsorption onto MTM-600 and Degussa P25 (71).

Both the fast and slow adsorption processes are slower in the case of MTM-600 compared with P25. The slower rate process is lower by a factor of about 2, while the faster rate process is slower by a factor of ≈11.

The mechanism of adsorption has been dealt with in another paper (72). Slow diffusion to the interface, followed by fast equilibration between outer- and inner-sphere surface complexes, is indicated by the data (eqs 5−7).

$$\equiv\mathrm{Ti{-}OH} + \mathrm{HL} \rightarrow \equiv\mathrm{Ti{-}OH{:}HL}; \quad k_{\mathrm{d}} \quad (5)$$

$$\equiv\mathrm{Ti{-}OH{:}HL} = \equiv\mathrm{Ti{-}L} + \mathrm{H_2O}; \quad K_{\mathrm{IS}} \quad (6)$$

$$\equiv\mathrm{Ti{-}OH{:}HL} \rightarrow \equiv\mathrm{Ti{-}OH} + \mathrm{HL};\ \text{k-d}; \quad k_{-\mathrm{d}} \quad (7)$$

The rate constants $k_1$ and $k_2$ are thus interpreted as $k_1 = k_d$ and $k_{-1} = K_{IS}k_{-d}$. The process is thus diffusion-controlled, with the rate of desorption being modulated by the stability of the inner-sphere complex ($K_{IS}$). Other recent work also supports the conclusion of diffusion control (73).

The P25 film is formed from particles that consist of aggregates of nanoparticles of 3 and 8 nm. It should be relatively easier for reactant molecules to navigate within the aggregated P25 particle mass than through a tortuous mesoporous network of microspheres with diameters of several hundreds of nanometers to micrometers. Thus, adsorption on the readily available sites (i.e., those closer to the solution) of MTM-600 is appreciably slowed down as compared to Degussa P25. Adsorption on less accessible sites is hindered by diffusion in both materials, and thus the above effect is less important: the values of $k_1(2)$ for MTM-600 and P25 differ only by a factor of 2. This difference may be attributed to the presence of pore bottle necks, which are likely to hinder molecular diffusion within the mesopore network.

**Table 2. Langmuir−Hinshelwood Rate Constants for the Adsorption of GA onto Degussa P25 and MTM-600**

| | Degussa P25 | MTM-600 |
|---|---|---|
| $k_1(1)$ [dm$^3$ mol$^{-1}$ s$^{-1}$] | $2.07 \times 10^5$ | $1.8 \times 10^4$ |
| $k_{-1}(1)$ [s$^{-1}$] | 4.1 | $3.7 \times 10^{-1}$ |
| $k_1(2)$ [dm$^3$ mol$^{-1}$ s$^{-1}$] | $1.18 \times 10^3$ | $5.2 \times 10^2$ |
| $k_{-1}(2)$ [s$^{-1}$] | $2.34 \times 10^{-2}$ | $1 \times 10^{-2}$ |

Both the maximum achievable degree of coverage and the kinetics of adsorption are crucial for the feasibility of use of novel mesoporous sorbents and catalysts. Detailed accessibility studies are underway in order to shed further light on such aspects.

Upon exposure to UV light, the intensity of the spectra of adsorbed GA decreases. A monotonous decrease in the absorbance is observed without indications of the formation of new species on the surface. A detailed analysis of the mechanism of GA photomineralization shall be published separately. Blanks performed without the $TiO_2$ film demonstrated that direct GA photodegradation was always less than 6% of the total degradation.

Figure 7 shows the time evolution of the GA FTIR signal for the MTM-*x* materials compared with that for Degussa P25 subject to heterogeneous photooxidation upon UV irradiation. The data show that the rate of photocatalytic decomposition increased steadily as a function of the temperature at which the MTM materials were calcined. The GA decomposition rate for the MTM-500 sample was slightly lower than that of P25, whereas that of MTM-600 was significantly superior. This difference between MTM-500 and MTM-600 is interesting because both solids have similar anatase

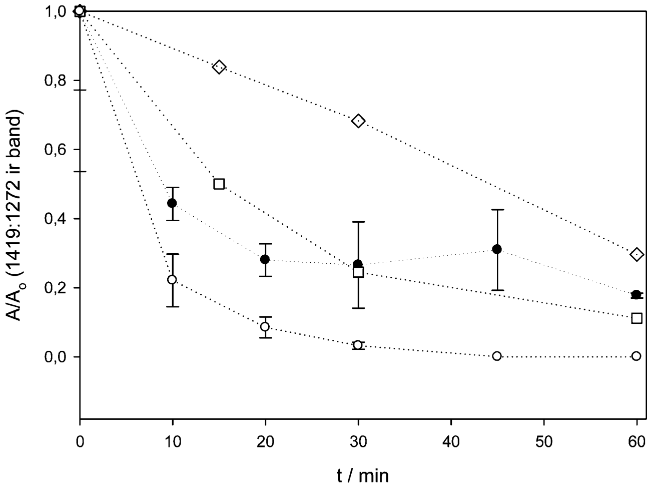

**FIGURE 7. Time evolution of the integrated 1419−1272 cm$^{-1}$ area during UV-light illumination of films. Films were prepared with 150 μL of a 20 g dm$^{-3}$ $TiO_2$ suspension: (◇) MTM-400; (□) MTM-500; (○) MTM-600; (●) Degussa P25. Initial GA concentration: 1.0 × 10$^{-4}$ mol dm$^{-3}$.**

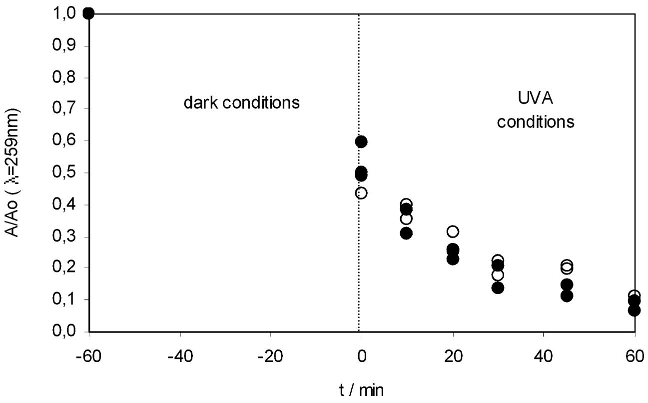

**FIGURE 8. Time evolution of the remnant GA concentration in solution (measured by UV−vis spectrometry), upon UV illumination in the presence of MTM-600 (○) and Degussa P25 (●).**

particle sizes, surface areas, and pore dimensions (see Table 1). It is conceivable that the MTM-600 sample has a higher proportion of anatase relative to amorphous material than MTM-500 because XRD cannot detect the latter. An alternate explanation refers to the little knowledge available concerning the actual adsorption sites that are photoactive; thermal treatment may either provide more sites or render the active sites even more reactive the active sites. Irrespective of the rationale, it is possible that further increases in the calcination temperature beyond 600 °C (not explored by us) could yield still further improvements in the degradation rates.

In contrast with the different rates of changes in surface speciation upon illumination, measurements in the aqueous phase demonstrate similar rates of decay of the GA concentration for MTM-600 and Degussa P25 (Figure 8). This behavior is probably due to the balance between the slower rates of replenishment of adsorbed GA onto MTM-600, together with the higher rate of photolytic destruction of the adsorbed material. Wang et al. (61) studied the photocatalytic degradation of methyl orange in slurries of MTMs prepared by a different route; only measurements of the solution contents were reported. Interestingly, the rate of degradation was higher than that observed in Degussa P25, even though the substrate molecule is rather large. The effect of annealing up to 450 °C was only modest. In light of our results, it is probable that annealing of the solid provided a better catalyst with a more limited accessibility.

In general, the present MTM-*x* materials, when calcined at sufficiently high temperatures (600 °C), showed excellent adsorbed GA decomposition rates, exceeding those that could be achieved with P25. This superiority is, in part, compensated for by a slower kinetics of mass transfer with the solution. The question that needs to be addressed here is, why should the kinetics of photodegradation in the thin film experiments be superior for MTM-600 compared with P25?

P25 is a mixed phase oxide comprised of 80% anatase nanoparticles with an average diameter of 25 nm and 20% rutile nanoparticles with an average diameter of about 80 nm (74). Anatase and rutile nanoparticles of these dimensions are expected to have band gaps ($E_g$) of 3.4 and 3.2 eV, respectively (50). On the other hand, the small anatase crystallites in MTM-600 have a diameter of only 12 nm, suggesting a band gap even more blue-shifted than that of anatase in P25. For illustration, Figure 9 compares the optical absorption edges of rutile and anatase nanoparticles of about these dimensions with emission from the lamp used in this study. As expected, the MTM-600 band gap is blue-shifted as compared to Degussa P25. However, the overlap with the lamp action spectrum largely negates the differences in light absorption. Furthermore, several other factors are important in determining the rates of photoinduced changes in the surface speciation. Examples of these factors are the amount and nature of the adsorbed species, charge carrier recombination rates (or charge trapping at the surface), and the rate of replenishment of GA from solution. Our results suggest that MTM-600 features either a higher number of photoactive sites or sites with enhanced photoactivity. It is important to note that charge recombination accounts for the fate of a great majority of the charge carriers and that adsorption of GA may affect this rate in an unpredictable fashion. We have demonstrated earlier that adsorption of oxalate *increases* the recombination rate on anatase, even though it generates a second channel that is photoactive. No such photoactive channel is present in rutile (75).

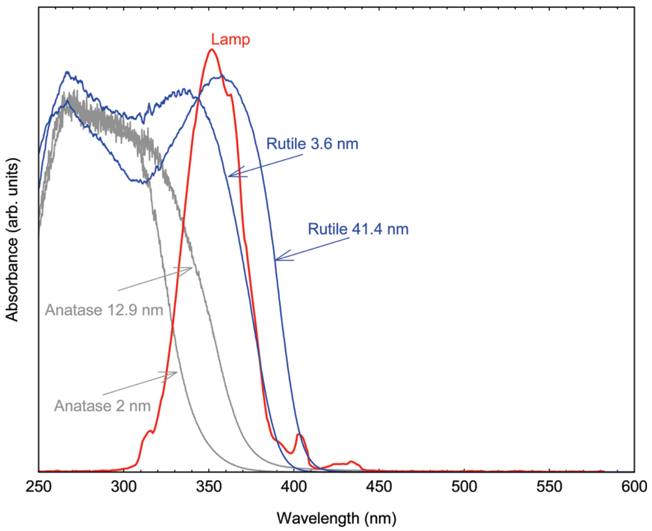

**FIGURE 9. Overlap of the optical absorption edges for anatase and rutile nanoparticles of different dimensions with the spectrum of the lamp used for the UV-A irradiation.**

The important point to stress is that surface photodecomposition is seen to be decoupled from solution removal (cf. behavior of MTM-600 and Degussa P25 in Figures 7 and 8). In a standard reactor, the enhanced surface photoactivity of MTM-600 is lost because of slower exchange kinetics in solution. Thus, the photon economy turns out to be similar in both cases (Figure 8).

This work has been carried out under standard conditions, i.e., in situ irradiation of the film−solution interface. The properties of MTM-*x* (especially MTM-600) described in this paper open, however, an attractive alternative. A two-stage decontamination reactor may be envisaged involving (rather slow) fixation in the adsorbed material at night and photodegradation of the wet adsorbed material under solar light. Conceptually, the separation stage of the mesoporous material should be easy to carry out, and the use of adsorbing and photocatalytic properties in separate stages would lead to a more efficient reactor. This concept shall be explored in the future (76). It would be particularly interesting to see if at still high calcination temperatures enhanced photoactivity can be achieved without a loss of porosity.

## CONCLUSIONS

A straightforward, continuous, and potentially scalable procedure has been employed to synthesize novel MTMs, the main structural characteristics of which have been described and discussed. The combination of a micronic particle size and large, accessible mesopores permits a high capacity of molecule adsorption, granting a highly available reactive area and diminishing diffusion times. It has been shown that the MTMs are good adsorbents and photocatalysts for the destruction of GA, comparing favorably with commercially available materials. It has also been shown that while adsorption on the microspheres is slower than that in the case of Degussa P25, adsorbed GA is destroyed faster. In addition, MTM colloids are easy to separate from a liquid phase because of their micronic size. Thus, these microsphere mesoporous materials have potential for use in photocatalytic reactors that rely on the concept of separate adsorption and photocatalytic destruction of organic pollutants, thus simplifying the development of solar reactors.

**Acknowledgment.** The authors thank Beatriz Molinari, Mariana Rosenbusch, and Elisabeth Drabarek for their help in characterization techniques. Work supported by the European Commission INCO Project ICA4-CT-2002-10001, Cost Effective Solar Photocatalytic Technology to Water Decontamination and Disinfection in Rural Areas of Developing Countries (SOLWATER), by Agencia Nacional de Promoción de Ciencia y Tecnología of Argentina (Grants PICT 06-13534, PICT 06-12122, and PICT 34518), and by Comisión Nacional de Energía Atómica (CNEA), under Projects P5-036-01 and P5-036-4 and a doctoral fellowship by CONICET to P.Z.A. is acknowledged.

**Supporting Information Available:** FTIR spectra of MTM-*x* samples and an MTM-400 sample after modification with dihexadecyl phosphate. This material is available free of charge via the Internet at http://pubs.acs.org.

## REFERENCES AND NOTES

(1) Fujishima, A.; Honda, K. *Nature* **1972**, *238*, 37.
(2) Fujishima, A. K.; Hashimoto, H. I. *Jpn. J. Appl. Phys.* **2005**, *44*, 8269.
(3) Linsebigler, A.; Lu, G.; Yates, J. *Chem. Rev.* **1995**, *95*, 735.
(4) Fox, M.; Dulay, M. *Chem. Rev.* **1995**, *83*, 341.
(5) Hoffmann, M. R.; Martin, S. T.; Choi, W. Y.; Bahnemann, D. W. *Chem. Rev.* **1995**, *95*, 69.
(6) Mills, A.; Le Hunte, S. *J. Photochem. Photobiol., A* **1997**, *108*, 135.
(7) Peral, J.; Ollis, D. *J. Mol. Catal. A: Chem.* **1995**, *115*, 347.
(8) Sanchez, B.; Coronado, J.; Candal, R.; Portela, R.; Tejedor, I.; Anderson, M.; Tompkins, D.; Lee, T. *Appl. Catal., B* **2006**, *66*, 295.
(9) Navntoft, C.; Araujo, P.; Litter, M.; Apella, M. C.; Fernandez, D.; Puchulu, M.; Hidalgo, M.; Blesa, M. *J. Sol. Energy Eng.* **2007**, *129*, 127.
(10) Duffy, E.; Al Touati, F.; Kehoe, S.; McLoughlin, O.; Gill, L.; Gernjak, W.; Oller, I.; Maldonado, M.; Malato, S.; Cassidy, J.; Reed, R.; McGuigan, K. *Sol. Energy* **2004**, *77*, 649.
(11) Meichtry, J.; Lin, H.; de la Fuente, L.; Levy, I.; Gautier, E.; Blesa, M.; Litter, M. *J. Sol. Energy Eng.* **2007**, *129*, 119.
(12) Alfano, O.; Bahnemann, D.; Cassano, A.; Dillert, R.; Goslich, R. *Catal. Today* **2000**, *58*, 199.
(13) Malato, S.; Blanco, J.; Alarcon, D.; Maldonado, M.; Fernandez-Ibañez, P.; Gernjak, W. *Catal. Today* **2007**, *122*, 137.
(14) Anpo, M.; Takeuchi, M. *J. Catal.* **2003**, *216*, 505.
(15) Ghosh, A. K.; Maruska, H. P. *J. Electrochem. Soc.* **1977**, *124*, 1516.
(16) Martin, S. T.; Morrison, C. L.; Hoffmann, M. R. *J. Phys. Chem.* **1994**, *98*, 13695.
(17) Lindgren, T.; Mwabora, J. M.; Avandaño, E.; Jonsson, J.; Hoel, A.; Granqvist, C.-G.; Lindquist, S.-E. *J. Phys. Chem. B* **2003**, *107*, 5709.
(18) Torres, G. R.; Lindgren, T.; Lu, J.; Granqvist, C. G.; Lindquist, S. E. *J. Phys. Chem. B* **2004**, *108*, 5995.
(19) Araujo, P. Z.; Mendive, C. B.; Rodenas, L. A. G.; Morando, P. J.; Regazzoni, A. E.; Blesa, M. A.; Bahnemann, D. *Colloids Surf. A* **2005**, *265*, 73.
(20) Hermann, J. M. *Catal. Today* **1999**, *53*, 115.
(21) Navntoft, C.; Wolfram, E.; Paladini, A.; Dawidowski1, L.; Blesa, M. A. *Av. Energías Renovables Medio Ambiente* **2006**, *10*, 11.
(22) Malato, S.; Fernández-Ibáñez, P.; Maldonado, M. I.; Blanco, J.; Gernjak, W. *Catal. Today* **2009**, *147*, 1.
(23) Bouras, P.; Stathatos, E.; Lianos, P. *Appl. Catal., B* **2007**, *73*, 5159.
(24) Choi, H.; Stathatos, E.; Dionysiou, D. D. *Thin Solid Films* **2006**, *510*, 107.
(25) Peng, T. Y.; Zhao, D.; Dai, K.; Shi, W.; Hirao, K. *J. Phys. Chem. B* **2005**, *109*, 4947.
(26) Wang, X.; Yu, J. C.; Ho, C.; Hou, Y.; Fu, X. *Langmuir* **2005**, *21*, 2552.
(27) Brinker, C. J.; Lu, Y.; Sellinger, A.; Fan, H. *Adv. Mater.* **1999**, *11*, 579.
(28) Yang, P.; Zhao, D.; Margolese, D. I.; Chmelka, B. F.; Stucky, G. D. *Chem. Mater.* **1999**, *11*, 2813.
(29) (a) Soler-Illia, G. J. A. A.; Louis, A.; Sanchez, C. *Chem. Mater.* **2002**, *14*, 750. (b) Crepaldi, E. L.; Soler-Illia, G. J. A. A.; Grosso, D.; Ribot, F.; Cagnol, F.; Sanchez, C. *J. Am. Chem. Soc.* **2003**, *125*, 9770.
(30) Kondo, J. N.; Yamashita, T.; Nakajima, K.; Lu, D. L.; Hara, M.; Domen, K. *J. Mater. Chem.* **2005**, *15*, 2035.
(31) Lu, Y. F.; Fan, H. Y.; Stump, A.; Ward, T. L.; Rieker, T.; Brinker, C. J. *Nature* **1999**, *398*, 223.
(32) Baccile, N.; Grosso, D.; Sanchez, C. *J. Mater. Chem.* **2003**, *13*, 3011.
(33) Tsung, C.-K.; Fan, J.; Zheng, N.; Shi, Q.; Forman, A. J.; Wang, J.; Stucky, G. D. *Angew. Chem., Int. Ed.* **2008**, *47*, 8682.
(34) Vasiliev, P. O.; Faure, B.; Ng, J. B. S.; Bergström, L. *J. Colloid Interface Sci.* **2008**, 144.
(35) Grosso, D.; Soler-Illia, G.; Crepaldi, E. L.; Charleux, B.; Sanchez, C. *Adv. Funct. Mater.* **2003**, *13*, 37.
(36) Beitollahi, A.; Daie, A. H. H.; Samie, L.; Akbarnejad, M. M. *J. Alloys Compd.* **2010**, *490*, 311.
(37) Gumy, D.; Rincon, A.; Hajdu, R.; Pulgarin, C. *Sol. Energy* **2006**, *80*, 1376.
(38) Carbajo, M.; Beltrán, F.; Medina, F.; Gimeno, O.; Rivas, F. *Appl. Catal., B* **2006**, *67*, 177.
(39) Mu, S. *Synth. Met.* **2003**, *139*, 287.
(40) Benítez, F. J.; Real, F.; Acero, J. L.; Leal, A. I.; García, C. J. *Hazard. Mater. B* **2005**, *126*, 3139.
(41) Saroj, D.; Kumar, A.; Bose, P.; Tare, V.; Dhopavkar, Y. *Water Res.* **2005**, *39*, 1921.
(42) Araujo, P. Z.; Morando, P. J.; Blesa, M. A. *Langmuir* **2005**, *21*, 3470.
(43) Angelome, P. C.; Soler-Illia, G. J. A. A. *J. Mater. Chem.* **2005**, *15*, 3903.
(44) Ahonen, P.; Tapper, U.; Kauppinen, E.; Joubert, J.; Deschanvres, J. *Mater. Sci. Eng., A* **2001**, *135*, 113.
(45) Huisman, C.; Goossens, A.; Schoonman, J. *Chem. Mater.* **2003**, *15*, 4617.
(46) Iskandar, F.; Gradon, L.; Okuyama, K. *J. Colloid Interface Sci.* **2003**, *265*, 296.
(47) Luca, V.; Osborne, M.; Sizgek, D.; Griffith, C.; Araujo, P. Z. *Chem. Mater.* **2006**, *18*, 6132.
(48) Baxendale, J. H.; Bridge, M. K. *J. Phys. Chem.* **1955**, *59*, 783.
(49) Socrates, G. *Infrared and Raman Characteristic Group Frequencies. Tables and Charts*, 3rd ed.; John Wiley & Sons Inc.: New York, 2001; p 347.
(50) Luca, V. *J. Phys. Chem. C* **2009**, *113*, 6367.
(51) Conde-Gallardo, A.; Guerrero, M.; Castillo, N.; Soto, A. B.; Fragoso, R.; Cabañas-Moreno, J. G. *Thin Solid Films* **2005**, *473*, 6873.
(52) Peng, T.; Zhao, D.; Dai, K.; Shi, W.; Hirao, K. *J. Phys. Chem. B* **2005**, *109*, 4947.
(53) Zhang, Y.; Li, J.; Wang, J. *Chem. Mater.* **2006**, *18*, 2917.

(54) Chaumonnot, A.; Tihay, F.; Coupé, A.; Pega, S.; Boissičre, C.; Grosso, D.; Sanchez, C. *Oil Gas Sci. Technol.* **2009**, *64*, 681.

(55) Soler-Illia, G. J. A. A.; Crepaldi, E. L.; Grosso, D.; Sanchez, C. *Curr. Opin. Colloid Interface Sci.* **2003**, *8*, 109.

(56) Grosso, D.; Cagnol, F.; Coupé, A.; Baccile, N.; Boissičre, C.; Soler-Illia, G. J. A. A.; Crepaldi, E. L.; Sanchez, C. *Mater. Res. Soc. Proc. Symp.* **2003**, *775*, 91.

(57) Grosso, D.; Cagnol, F.; Soler-Illia, G. J. A. A.; Crepaldi, E. L.; Amenitsch, H.; Brunet-Bruneau, A.; Bourgeois, A.; Sanchez, C. *Adv. Funct. Mater.* **2004**, *14*, 309.

(58) Soler-Illia, G. J. A. A.; Innocenzi, P. *Chem.—Eur. J.* **2006**, *12*, 4478.

(59) Boissière, C.; Grosso, D.; Amenitsch, H.; Gibaud, A.; Coupé, A.; Baccile, N.; Sanchez, C. *Chem. Commun.* **2003**, 2798.

(60) Imperor-Clerc, M.; Davidson, P.; Davidson, A. *J. Am. Chem. Soc.* **2000**, *122*, 11925.

(61) Wang, Y.; Jiang, Z.; Yang, F. *Mater. Sci. Eng., B* **2006**, *128*, 229.

(62) Kruk, M.; Jaroniec, M. *Chem. Mater.* **2003**, *15*, 2942.

(63) Kim, T. W.; Ryoo, R.; Kruk, M.; Gierszal, K. P.; Jaroniec, M.; Kamiya, S.; Terasaki, O. *J. Phys. Chem. B* **2004**, *108*, 11480.

(64) Ravikovitch, P. I.; Neimark, A. V. *Langmuir* **2002**, *18*, 9830.

(65) Kirsch, B. L.; Richman, E. K.; Riley, A. E.; Tolbert, S. H. *J. Phys. Chem. B* **2004**, *108*, 12698.

(66) Choi, S. Y.; Mamak, M.; Speakman, S.; Chopra, N.; Ozin, G. A. *Small* **2005**, *1*, 226.

(67) Angelome, P. C.; Soler-Illia, G. J. A. A. *Chem. Mater.* **2005**, *17*, 322.

(68) Reyes, S. C.; Sinfelt, J. H.; DeMartin, G. J. *J. Phys. Chem. B* **2000**, *104*, 5750.

(69) Jovice, B. S. N.; Kamali-Zare, P.; Sörensen, M.; Brismar, H.; Hedin, N.; Bergström, L. *Langmuir* **2010**, *26*, 466.

(70) (a) Rudzinski, W.; Plazinski, W. *J. Phys. Chem. C* **2007**, *111*, 15100. (b) Plazinski, W.; Rudzinski, W. *Langmuir* **2010**, *26*, 802.

(71) Araujo, P.; Martinez, E. D.; Morando, P. J.; Blesa, M. A. Unpublished results, 2009.

(72) Roncaroli, F.; Blesa, M. A. *Phys. Chem. Chem. Phys.* **2010**, in press.

(73) Young, A. G.; McQuillan, A. J. *Langmuir* **2009**, *25*, 3538.

(74) Martra, G. *Appl. Catal., A* **2000**, *200*, 275.

(75) Mendive, C. B.; Bredow, Th. K. M.; Blesa, M. A.; Bahnemann, D. Unpublished.

(76) Carp, O.; Huisman, C. L.; Reller, A. *Prog. Solid State Chem.* **2004**, *32*, 33.

AM100188Q